

# Scaling behaviors in simulated collagen fibrils

Robert Bertoldo Tavares<sup>1</sup>, Michael Ferreira de Souza<sup>2</sup>, Béla Suki<sup>3</sup>, and Ascânio Dias Araújo<sup>1,2,\*</sup>

<sup>1</sup>UFC, Departamento de Física, Universidade Federal do Ceará, Fortaleza, Ceará, Brasil

<sup>2</sup>UFC, Departamento de Estatística e Matemática Aplicada, Universidade Federal do Ceará, Fortaleza, Ceará, Brasil

<sup>3</sup>BU, Department of Biomedical Engineering, Boston University, Boston, MA, USA

\*Correspondence: ascanio@fisica.ufc.br

**ABSTRACT** Collagen fibrils are hierarchical protein assemblies that provide tensile strength and structural support to mammalian tissues. Understanding the relationship between assembly kinetics, structural organization, and mechanical properties is fundamental to soft matter physics and biomaterials science. Here, we investigate collagen fibril formation and mechanical failure through complementary computational models: a diffusion-limited aggregation (DLA) algorithm with lateral surface diffusion that simulates the entropy-driven self-assembly process, and a probabilistic fracture mechanics model. Fibril assembly is governed by a surface diffusion parameter  $T_s$  that represents the molecular mobility and rearrangement capability of collagen molecules after initial attachment. Increasing  $T_s$  drives a morphological transition from open, fractal structures (fractal dimension  $D_f \approx 1.71$ , characteristic of DLA) to dense, compact fibrils ( $D_f \approx 1.96$ , approaching Euclidean space-filling). Critically, we find that  $D_f$  is a robust predictor of both tensile strength and failure mode: higher  $D_f$  corresponds to enhanced load-bearing capacity through increased connectivity of the active skeleton. Mechanical failure proceeds via avalanche-like rupture events whose size distributions follow power-law scaling, with exponents that depend systematically on  $T_s$ . Notably, these scaling exponents exhibit two distinct linear regimes when plotted against  $\log(T_s)$ , indicating a transition in the dominant failure mechanism between diffusion-limited and compact packing regimes. These findings establish fractal dimension as a quantitative link between assembly conditions and mechanical resilience, providing a framework for understanding how molecular-scale processes during self-assembly determine the emergent mechanical properties of hierarchical biomaterials.

**SIGNIFICANCE** Understanding collagen fibril formation and damage is crucial, because collagen fibrils are fundamental to the integrity of virtually all tissues. This study reveals that the fracture process in simulated collagen fibrils is governed by avalanches and power laws with well-defined exponents. More importantly, the results demonstrate that the fractal dimension of fibril cross-section is a robust indicator of both the mechanical properties and the failure mode of collagen fibrils.

## INTRODUCTION

Type I collagen is a fibrillar protein found in nearly all mammalian extracellular matrices (ECM), providing structural support for cells and tissues. Collagen fibrils are key components of various body structures, including skin, tendons, bone, cartilage, and the cornea (1–7). These structures rely on collagen to provide elasticity, tensile strength, and resilience against mechanical stresses (1, 8). Collagen molecules have a characteristic rod-like shape, with dimensions of approximately 300 nm in length and 1.5 nm in diameter (1, 9). These molecules naturally assemble into elongated fibrillar structures that can grow up to 500  $\mu\text{m}$  in length and 500 nm in diameter (10–12). The fibrils, in turn, form fibers, which can reach diameters ranging from 1 to 20  $\mu\text{m}$ . This hierarchical organization enables collagen structures to store and transmit mechanical energy generated by muscle contraction and movement (7, 13).

Studying the structure and mechanical properties of collagen fibrils is challenging, especially at the nanoscale (14). Experimental techniques such as atomic force microscopy (AFM) have provided valuable insights into the morphology and behavior of isolated fibrils under tension. For example, Van der Rijt et al. used AFM to measure the mechanical properties of tendon fibrils, evaluating their tensile behavior until failure (15). Similarly, Svensson et al. (16) developed a technique using a piezoelectric actuator and a cantilever to measure stress and strain during uniaxial stretching of fibrils. However, these experimental techniques have limitations when resolving small-scale forces and the collective behavior of molecules within

the fibrils under stress (17). Given the hierarchical complexity of collagen fibers and the limitations of experimental methods, computational models play a crucial role in studying these structures, enabling the exploration of their intrafibrillar organization and mechanical behavior under a wider range of conditions.

Several models have been developed to study the mechanical behavior of fibrils and fibers. Buehler et al. introduced a coarse-grained molecular dynamics framework that models large molecules as particles, while Depalle et al. offered valuable insights into fibril elasticity and the effects of mineral incorporation on mechanical stability under stress or degradation (18–22). Araujo et al. developed an anisotropic random-walk model coupled with binding-unbinding reactions to describe how enzymatic digestion alters fibril and tissue elasticity (23). In addition, Deng et al. showed that fibril waviness contributes to fiber modulus, providing insights into the interaction between enzyme activity and mechanical forces on collagen fibers (24). While these models have advanced the understanding of collagen mechanics at the molecular level, they do not address important features of fibril behavior, such as their fractal organization and the collective dynamics of rupture events, which are essential for understanding how fibrils respond to mechanical stresses during failure.

In this work, we aimed to address gaps in current models by studying the fractal properties of collagen fibrils and the collective behavior of their failure processes. We adopted a modified Diffusion-Limited Aggregation (DLA) model with lateral diffusion to simulate the formation of fibrils with morphologies analogous to real collagen fibrils (25). Using this model, we analyzed how the fractal structure influences the mechanical strength and resilience of fibrils. Furthermore, we established that fibril rupture occurs via avalanches, allowing us to identify scaling laws that govern the distribution of microscopic failure events.

This study consisted of two main parts. In the first part, we simulated the formation of collagen fibrils using a modified diffusion-limited aggregation (DLA) method. In the second part, we analyzed the structural and failure properties of the generated fibrils.

## Fibril Formation Model

Collagen fibril formation was modeled using a three-dimensional diffusion-limited aggregation (DLA) algorithm, implemented on a cubic lattice. Collagen molecules were represented as rigid rods, specifically modeled as rectangular bars with dimensions  $L_x = 1$ ,  $L_y = 18$ ,  $L_z = 1$  in lattice units (l.u.). The primary length of the collagen molecules,  $L_y = 18$ , was selected as the characteristic length for all spatial dimensions in the model.

The aggregation process starts by placing the first molecule at the center of the lattice, our diffusion domain. Subsequent molecules are released one at a time, from random positions on a sphere with radius  $R$ , centered at the origin. The value of  $R$  is dynamically updated to reflect the maximum extent of the growing aggregate along the  $y$ -axis. Each released molecule then performs a random walk on the lattice until one of the following conditions is met:

1. The molecule attaches to the existing aggregate;
2. The molecule is discarded if it exceeds a distance greater than  $2R$  from the center of the lattice.

Once a molecule attaches and the fibril grows, the value of  $R$  is recalculated. For simplicity, molecular rotation during the random walk is not allowed. This iterative cycle of release, diffusion, and potential attachment of molecules continues until the aggregate reaches the desired size, limited here to 30,000 molecules.

The molecular diffusion process is modeled by a three-dimensional random walk on a cubic lattice. In the  $z$ - $x$  plane, molecules can move to first-neighbor sites (distance = 1 l.u.) or second-neighbor sites (distance =  $\sqrt{2}$  l.u., i.e., diagonal movements). Along the  $y$ -axis, movement is restricted to first-neighbor sites only (distance = 1 l.u.). In real collagen molecules, lateral aggregation occurs with a characteristic spacing of 67 nm between positions (11), which leads to specific positions where a new molecule can be incorporated into the growing aggregate. In our model, molecular attachment is restricted to multiples of 4 l.u. along the  $y$ -axis (25).

The formation of real fibrils is driven by electrostatic forces (25), causing the molecules to seek to minimize their exposed surfaces (25, 26). To mimic this process, we implemented a lateral diffusion algorithm, which follows the same random walk steps as the previous process, but with no movement along the  $y$ -axis. This additional degree of freedom allows a newly aggregated molecule to explore the surface and find a position that minimizes its exposed area (27). If multiple positions minimize the exposed surface area, the molecule remains in the first one found. The number of attempts for the molecule to explore the surface is given by the parameter  $T_s$  (25). Using this algorithm, we statistically generated 50 fibrils, each containing at least 30,000 rods, considering different values of  $T_s$ . Varying the  $T_s$  parameter allowed us to investigate its impact on both the compactness and structural properties of the fibril, as well as the mechanical response of fibrils generated with different  $T_s$  when subjected to external stresses.

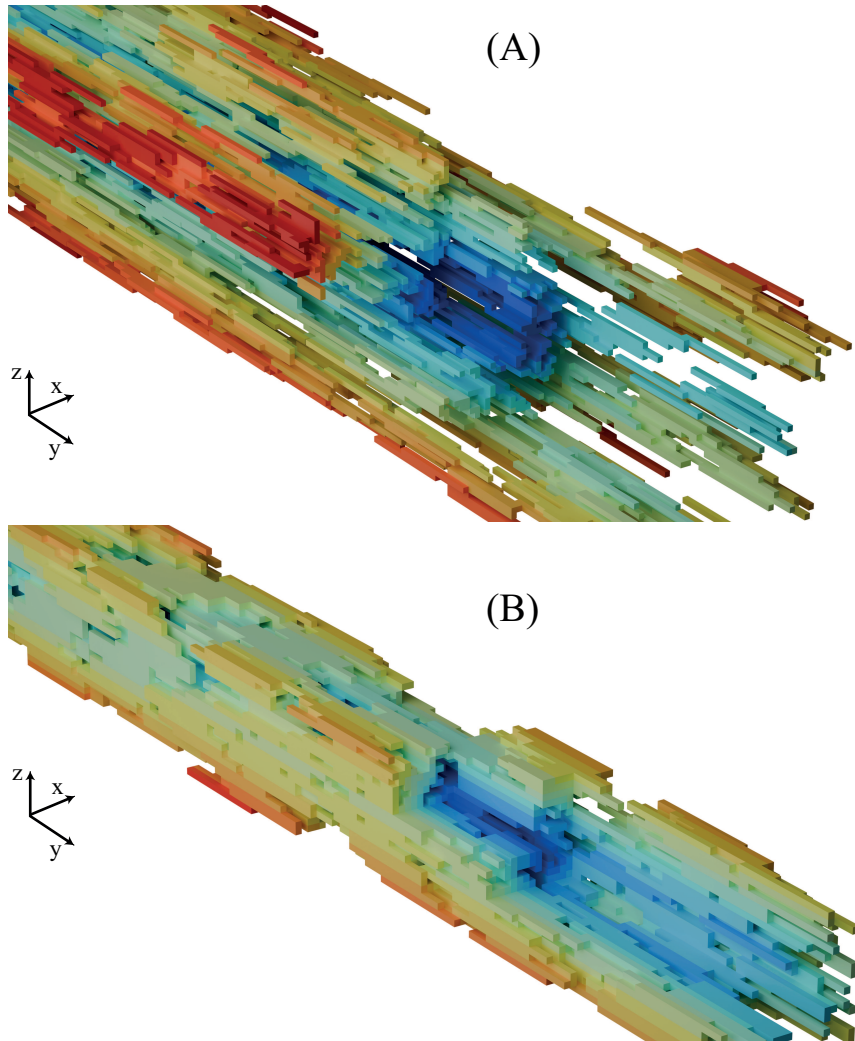


Figure 1: Representation of part of the fibrils generated with the DLA algorithm containing 30,000 molecules. The different fibrils shown in *A* and *B* were obtained using different values of the parameter  $T_s$ . In (*A*), the fibril was generated with  $T_s = 2$ , indicating short-term diffusion, while in (*B*),  $T_s = 8192$ , representing the effect of long-term diffusion. The colors indicate the time of attachment of each molecule to the aggregate. The closer the color is to blue, the earlier the molecule was attached to the aggregate, while a trend towards red indicates more recent additions.

The generated fibrils exhibit complex structures with numerous internal voids. In Fig. 1, we present two collagen fibrils generated with our model, each composed of 30,000 rod-like objects representing single collagen molecules. Both structures exhibit morphological features consistent with real fibrils, including hierarchical packing patterns. The key difference arises from the diffusion parameter  $T_s$ . Higher values of  $T_s$  lead to a significant reduction in internal voids, resulting in a more compact and homogeneous structure, as illustrated in Fig. 1. Panels *A* and *B* show typical fibrils formed with  $T_s = 2$  and  $T_s = 8192$ , respectively. For  $T_s = 2$ , the fibril displays a more hollow architecture with visible gaps between molecular clusters, while for  $T_s = 8192$ , the structure becomes densely packed with minimal internal spaces. The color gradient—from blue to yellow to red—represents the relative age of the incorporated segments, with blue indicating early and red indicating more recent additions.

The fibril's growth occurs anisotropically, with preferential elongation along the  $y$ -axis. To understand the influence of the parameter  $T_s$  on radial packing, we implemented a growth model focused on a specific fibril region, termed the central segment. We selected the region ( $-100 \leq y \leq 100$ ) of a fully formed fibril and performed additional molecular deposition exclusively within this region. Newly released molecules are released from a cylindrical surface surrounding the segment and diffuse inward until encountering the existing aggregate, following the same random walk, binding, and surface rolling rules previously described. This approach allows us to systematically thicken the fibril cross-section and isolate the structural effects

of  $T_s$  on lateral packing. Growth of the central segment was continued until the average radius across all transverse sections reached 100 l.u. Fig. 2 shows the resulting projected central segment (in the  $x$ - $z$  plane) for different values of  $T_s$ .

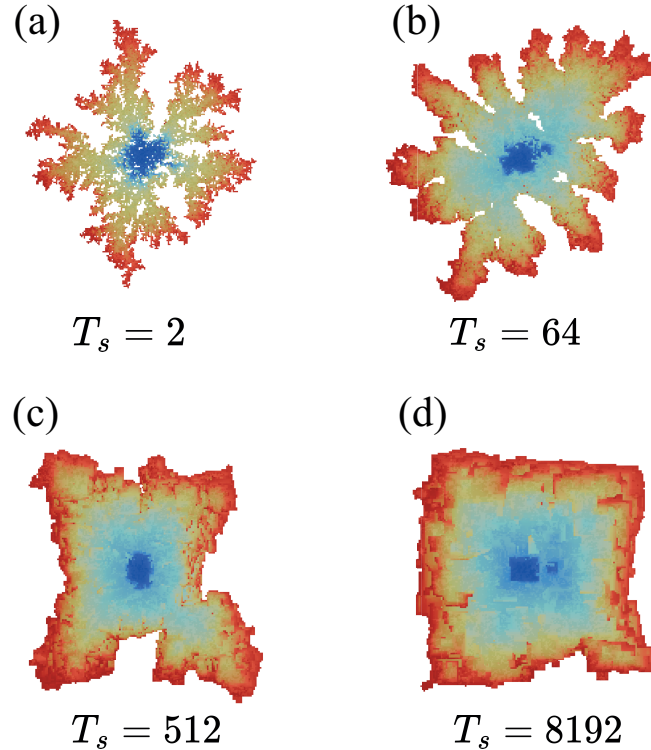


Figure 2: Representative examples of projected central segments ( $x$ - $z$  plane) for different values of  $T_s$ : (a)  $T_s = 2$ , (b)  $T_s = 64$ , (c)  $T_s = 512$ , and (d)  $T_s = 8192$ . The progression illustrates a clear structural transition from sparse, irregular morphology at low  $T_s$  to dense, radially symmetric packing at high  $T_s$ . The color gradient (from blue to yellow to red) represents the temporal sequence of molecular incorporation, with blue indicating early-attached molecules and red denoting recent additions.

Fig. 2 clearly illustrates the effects of the parameter  $T_s$  on the central segment. At low  $T_s$  (Fig. 2a), the projected structure exhibits an open, branched architecture with sparse packing. As  $T_s$  increases, growth becomes progressively more compact and regular, reaching its most uniform configuration at  $T_s = 8192$  (Fig. 2d). Since the number of intermolecular bonds depends directly on local molecular density, this structural transition from open to compact packing suggests enhanced mechanical stability. We hypothesize that increasing  $T_s$  strengthens the fibril's resistance to external forces by increasing the local coordination number, thereby creating a more cohesive network (28).

To quantify how  $T_s$  modulates fibril structure, we analyzed the fractal dimension of the central segments. For each value of  $T_s$ , we generated 50 independent central segments following the growth model described above. We performed transverse cross-sectional cuts along the  $y$ -axis, spanning from  $y = -90$  to  $y = 90$  at intervals of 18 l.u., yielding 11 sections per central segment. For each cross-section, we identified the center of mass and determined the maximum radius  $R_{\max}$  enclosing all particles in that section. We then measured the mass  $m(R)$ , defined as the number of particles within a circular region of radius  $R$  centered at the cross-section's center of mass, for a series of radii ranging from a minimum value, from  $R_{\min} = 5$  l.u. to  $R_{\max}$ . We computed the mean mass at each radius by averaging over all 550 cross-sections (11 sections  $\times$  50 central segments) (29). The fractal dimension  $D_f$  was then extracted from the mass-radius scaling relation (30):

$$m(R) \sim R^{D_f}, \quad (1)$$

by performing a linear fit on a log-log plot.

As shown in Fig. 3, the fractal dimension  $D_f$  reveals a pronounced dependence on  $T_s$ , providing quantitative evidence for the morphological transition observed in Fig. 2. For the lowest value tested,  $T_s = 2$ , we observe  $D_f = 1.708 \pm 0.005$ , in excellent agreement with the characteristic value of two-dimensional diffusion-limited aggregation ( $D_f \approx 1.71$ ) (31), consistent with the sparse, branched structure seen in Fig. 2a. As  $T_s$  increases,  $D_f$  rises sharply, saturating at  $D_f = 1.963 \pm 0.001$  for  $T_s = 8192$ .

This saturation value approaches the Euclidean limit of  $D_f = 2.0$  for a fully compact two-dimensional disk, reflecting the dense, symmetric morphology observed in Fig. 2d. This progression quantitatively confirms a clear structural transition from fractal, diffusion-limited growth to nearly space-filling, compact packing as the diffusion parameter increases.

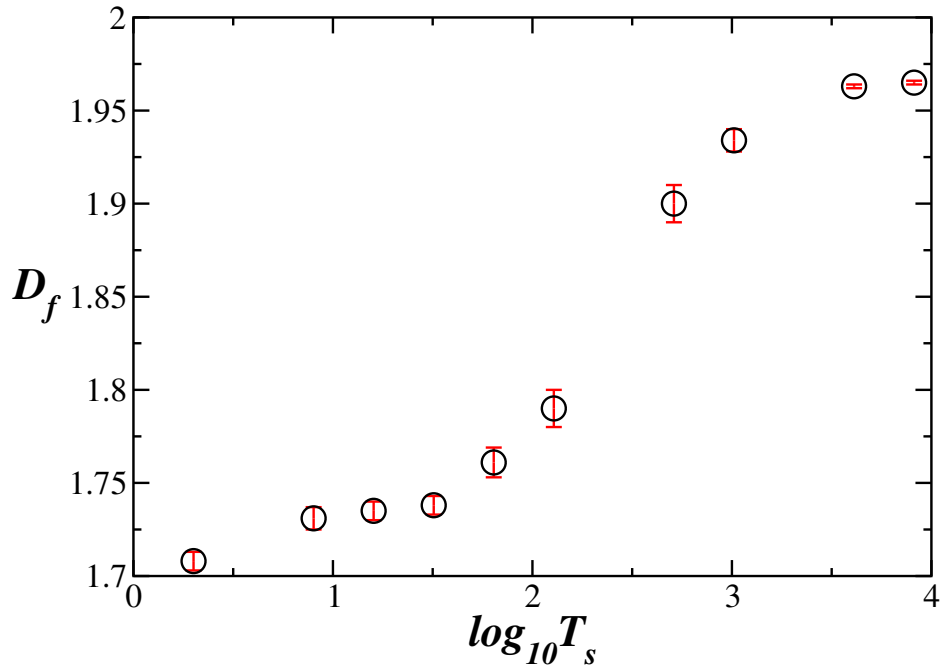


Figure 3: Average fractal dimension  $D_f$  as a function of the diffusion parameter  $T_s$  in a linear-log scale. Error bars are shown in red. The fractal dimension increases from  $D_f = 1.708 \pm 0.005$  at  $T_s = 2$  to  $D_f = 1.963 \pm 0.001$  for  $T_s = 8192$ .

## Mechanical Model for Fibril Rupture

Since the collagen molecules are modeled as rigid rods that do not undergo continuous deformation under stress prior to rupture, a deterministic fracture simulation is not feasible. We therefore employed a probabilistic framework, a conventional method for modeling failure in disordered systems (32–34). In this framework, failure occurs through the random removal of bonds between fundamental units, with the probability of bond breakage depending on whether the applied force exceeds a threshold value. Thus, entire molecules (rigid rods that constitute the primary structural units) are removed from the fibril according to a probability function. The model was implemented according to the following steps: (i) Identify the trunk (the force-carrying core at the left end) in the middle of the fibril with dimensions  $S_x = 17$ ,  $S_y = 201$  and  $S_z = 17$  l.u. (35). Inevitably, the removal of part of the fibril for rupture analysis results in regions that remain part of the fibril but consist of disconnected molecules (dangling ends), which do not contribute to force transmission (36). This detail leads us to our next step, (ii) identifying the force-carrying active skeleton (backbone) prior to applying tensile tests (37).

In order to do that, we mark all molecules that have a segment in the first cross-sectional area, designated by  $y = 1$ , as active. The identification process proceeds for each cross-sectional area along the isolated trunk, where each molecule belongs to the cross-sectional area that is marked. This process continues until it reaches the last cross-sectional area located at  $y = S_y$ . Once the last cross-sectional area is analyzed, the procedure is reversed, starting from  $y = S_y$  and moving back toward  $y = 1$ , considering only those molecules previously marked as active. At the end, only molecules with structural connectivity remain, forming the final backbone (35). The steps of this process are illustrated in Fig. 4.

With the backbone identified, we can simulate a tensile test by incrementally applying an external force  $F$  along the main axis ( $y$ ). To translate this force into local stress, we evaluate at each cross-section along the backbone the effective support area, i.e., the area occupied by the molecules. Collagen molecules are modeled as rigid rods of length  $L_y = 18$ , therefore, each cross-section containing a molecule includes a one-unit-long discrete segment, and each of these segments is assumed to have unit-area (25). Thus, for cross-section  $i$ , the effective force-carrying area is the number of segments  $N(i)$  that are part of the skeleton. For simplicity, we assume that  $F$  is uniformly distributed among these units, the local stress at a cross-section  $i$  is given by (35):

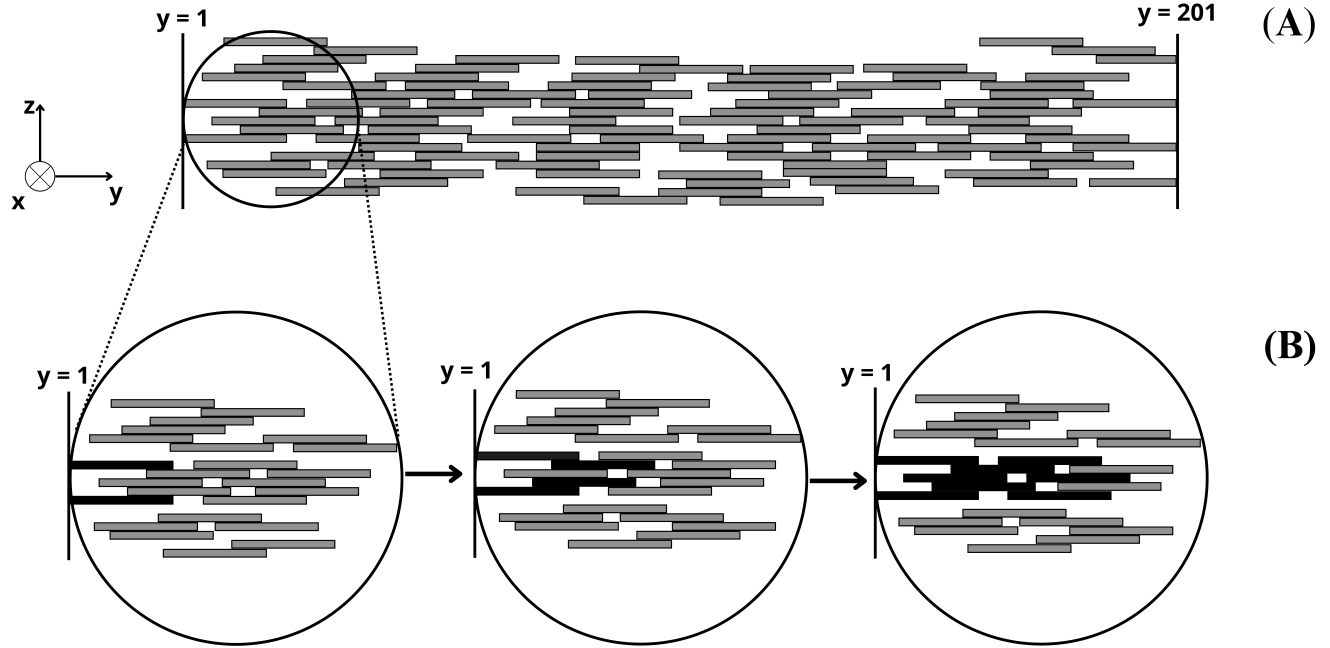


Figure 4: (A) A typical two-dimensional visualization of the fibril trunk, which is selected and isolated from the entire fibril to identify the force-carrying active skeleton. The circle highlights the region where the identification process starts. (B) Step-by-step procedure for identifying the active skeleton, from left to right. As we proceed, the active portion of the trunk is highlighted in black. This continues until the opposite end is reached and the entire backbone is identified. At the end of this process, only the structure referred to as the conductive skeleton remains, allowing us to proceed with the analysis of the fracture process.

$$\sigma(i) = \frac{F}{N(i)}. \quad (2)$$

For simplicity, we assume that structural failure occurs through the breakage of intermolecular bonds, leading to the removal of entire molecules from the backbone—not by isolated segments. This assumption is based on the fact that the internal bonds between segments that compose the molecule exceed the strength of intermolecular forces (35). In other words, we explicitly assume that intermolecular bonds fail but the collagen molecule itself never ruptures; instead, it is removed as a whole intact unit. To decide probabilistically on this removal, we first calculate the average stress acting on each molecule. Since the molecule extends over multiple cross-sections, the average stress on a molecule,  $\sigma_M$ , is obtained by the mean of the local stresses  $\sigma(i)$  across the  $n$  cross-sections that contain the molecule (35):

$$\sigma_M = \frac{1}{n} \sum_{i=1}^n \sigma(i). \quad (3)$$

A molecule's fracture resistance is related to the number of intermolecular bonds it forms within the backbone (38). In an attempt to quantify this resistance for a given molecule, we calculate the number of first neighbors for each segment at every cross-section containing the molecule. These values are then summed across all relevant layers, yielding the total number of contacts the molecule makes with its neighbors  $K$ . The total resistance is then  $K$  times  $\sigma_c$ , where  $\sigma_c$  is the critical stress for bond rupture, which is taken as unity, assuming the fibril is composed of identical molecules.

Finally, we define the probability to remove a single molecule as:

$$P_R = \left( \frac{\sigma_M}{K\sigma_c} \right)^m, \quad (4)$$

where  $m$  is a constant that is related to the Weibull modulus (35, 39). Here, we adopt  $m = 2$ , characterizing a moderate level of stochasticity in fracture resistance (35). Fig. 5 shows how the probability to remove a single molecule is calculated. The analyzed molecule is shown in blue, and the calculation is performed considering the applied force  $F$ . Namely, we calculate the

stress  $\sigma(i)$  on each segment that is part of the molecule (blue pieces). The stress on a segment  $\sigma_i$  is a fraction of the total stress supported by each molecules belonging to this cross-section. The total stress on a molecule  $\sigma_M$ , is the average value of the stresses over all segments comprising the molecule. Finally, we can use the probability equation above to decide whether the molecule will be removed.

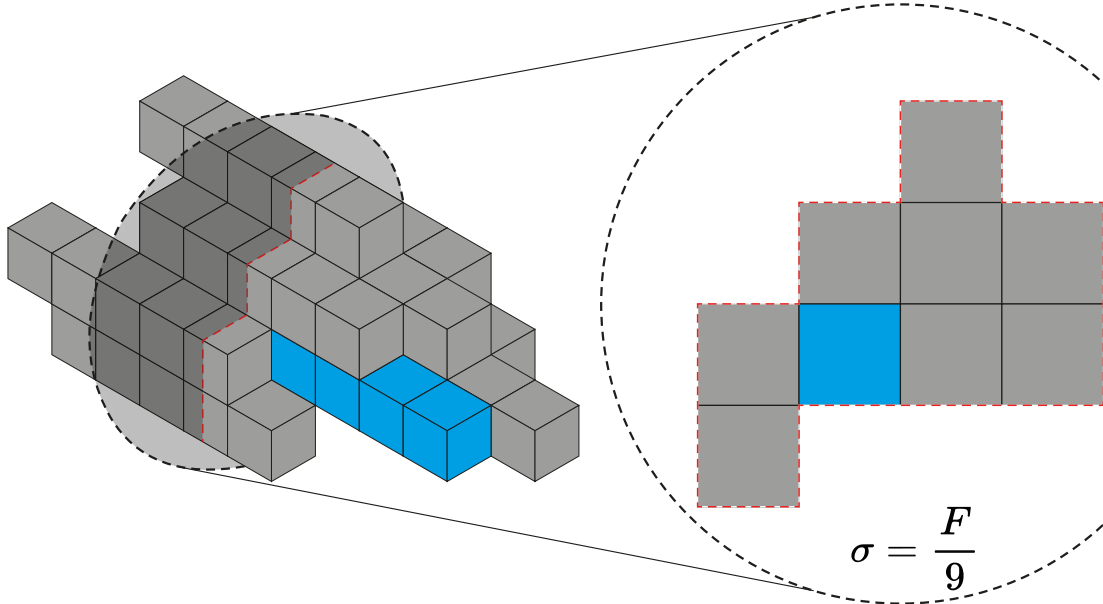


Figure 5: The left panel shows a segment of the backbone in which each rectangular bar denotes a single molecule. For simplicity, all molecules are assumed to have only five sections for visualization purposes. The molecule of interest—highlighted in blue—has its removal probability evaluated according to Eq. 4. To obtain the relevant quantities, we first calculate the tensile stress,  $\sigma$ , on every cross-section that cuts through that molecule. For illustrative clarity, we single out the first such section: it is depicted as a semi-transparent plane slicing through the blue block, while the red dashed contour traces the exact line where the plane intersects the fibril. The right panel demonstrates the arrangement of the selected molecule in the cut plane; under the applied force  $F$ , the stress is assumed to be distributed uniformly over the nine constituent segments, giving  $\sigma = \frac{F}{9}$ . The blue molecule forms three bonds with first-neighbor units, thereby fixing its coordination number. Repeating the same analysis for each cross-section that intersects the blue molecule yields the complete set of local values required for the determination of  $\sigma_M$  and  $K$ .

The removal probability  $P_R$  is then calculated from Eq. 4 for each molecule and compared with a random number between 0 and 1 associated with each molecule; if this random number is less than  $P_R$ , the molecule is removed. This procedure is then repeated for all molecules in the aggregate. After the first sweep, with the force  $F$  held constant, the removal probability  $P_R$  is recalculated for the remaining molecules, new random numbers are generated, and the system is examined for additional breakages. This process is repeated iteratively until no more breakages occur. The force is subsequently increased by half a unit, and the procedure is repeated. Fibril rupture is defined as the occurrence of a completely void cross-section, signifying the failure of the load-bearing skeleton. These steps in the removal process are schematized in Fig. 6, where in (A) the fibril is under stress, in (B) some molecules (blocks) have already been severed, and in (C) the rupture limit of the fibril was reached in the damaged region highlighted by the vertical solid lines. Throughout the process, the molecules removed at each applied force level were recorded.

Since our rupture model is probabilistic, for each value of  $T_s$  we selected 10 distinct fibrils and ran 1,000 independent rupture simulations on each. During these simulations, increasing force levels were applied, and at each level, we recorded the number of molecules removed from the fibril skeleton as well as those remaining attached.

To quantify the mechanical resistance of the simulated fibrils, we implemented a progressive failure model under an incrementally applied axial force (35). The evolution of the average fraction of removed molecules, denoted by  $\varphi$ , as a function of the applied force  $F$ , was analyzed for different values of the parameter  $T_s$ , as shown in Fig. 7(A). We observe that  $\varphi$  increases as a function of the applied force  $F$ . As force is applied, intermolecular bonds between molecules are progressively broken, leading to the gradual removal of molecules and, consequently, the loss of structural integrity.

As we can see from Fig. 7(A), the force threshold for rupture increases as a function of the parameter  $T_s$ . However, all

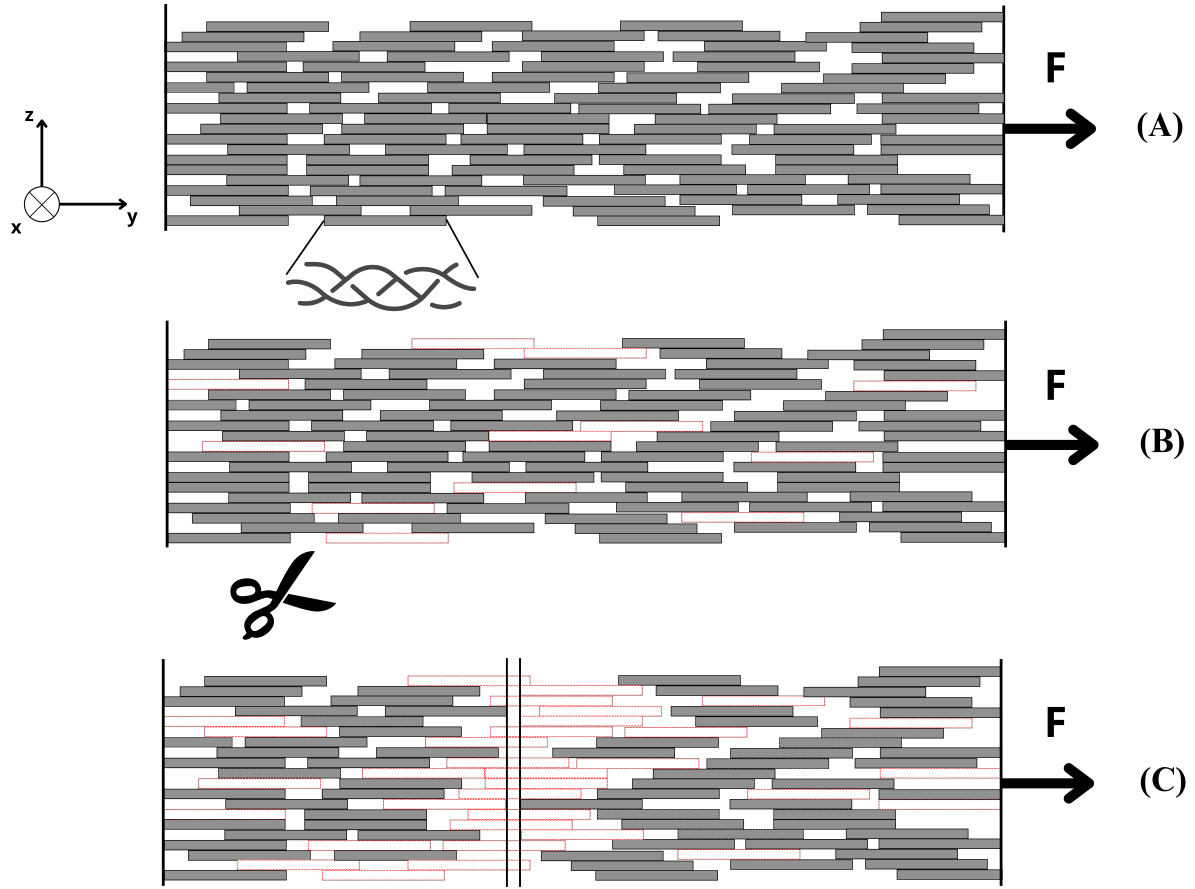


Figure 6: Schematic view of the fibril backbone and the stages of the rupture process. Panel (A) presents a 2D view of the backbone, with one of its ends subjected to an external force  $F$  applied along the  $y$ -axis. Each molecule (represented by gray rectangles) has a removal probability  $P_R$ , described by Eq. 4. The rupture process is evaluated statistically, molecule by molecule: when a randomly chosen value is less than the probability  $P_R$  of a molecule, it is removed from the aggregate, as shown in (B). As the applied force increases, the backbone undergoes progressive damage, as seen in (C). When a cross-section of the backbone becomes completely empty, marked by the solid lines, the aggregate breaks completely, reaching its maximum load-bearing limit.

curves exhibit a common functional form, which can be described by the following expression:

$$f(x) = (1 \times 10^{-3})[\exp(\beta x) - 1 + x^\alpha], \quad (5)$$

where the coefficients  $\alpha$  and  $\beta$  are determined from the fit to the data. First, at low force levels, the fibril aggregate shows minimal response, with few or no molecular removals. For low forces, as the applied force increases, the fraction of removed molecules,  $\varphi$ , is dominated by the power-law term. This leads to accelerated and cumulative damage to the backbone, creating weaknesses that facilitate the detachment of significant molecular clusters as the force continues to rise. At a critical stage, damage propagation intensifies sharply, with the exponential term gaining prominence and dominating the growth of  $\varphi$ . As a result, the fibril rapidly approaches its mechanical limit and ultimately ruptures (40). In Fig. 7(B) and Fig. 7(C), we show the behavior of the coefficients  $\beta$  and  $\alpha$ , respectively, as a function of the logarithm of  $T_s$ . Both coefficients exhibit a decreasing trend, stabilizing for  $T_s \geq 512$ . These coefficients characterize the fibril's resistance to gradual and explosive damage. The coefficient  $\alpha$  determines the rate of the power-law term, which is associated with gradual damage; lower values of  $\alpha$  reduce the rate of this damage progression (41). The coefficient  $\beta$ , in turn, modulates the exponential term, influencing explosive damage, with smaller values of  $\beta$  delaying its contribution to the rupture process (42, 43).

During the rupture process, the removal of a molecule creates a zone of weakness within the fibril, increasing the likelihood of subsequent molecular detachments and triggering a cascade of breakages. We observe that molecules detach either individually or in clusters. Here, we define a cluster as any group of two or more adjacent molecules that are removed following the same

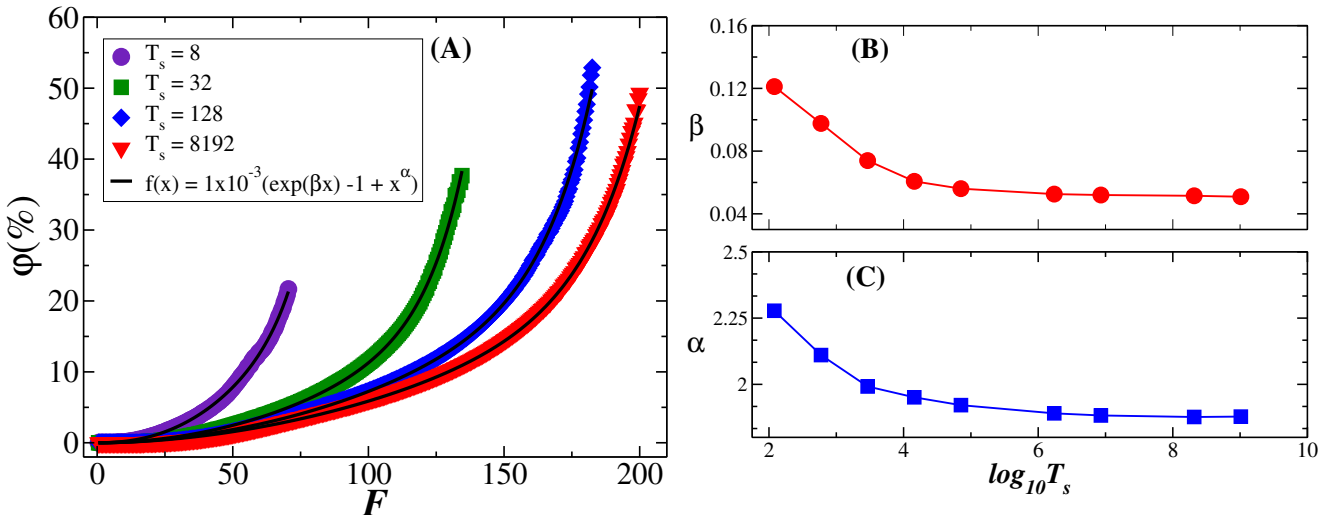


Figure 7: (A) The average fraction of removed molecules  $\varphi$  as a function of the applied force  $F$  until the fibril reaches the rupture limit for  $T_s = 8, 32, 128$  and  $8192$ . Despite varying the force thresholds for rupture, all curves are well described by the same functional form:  $f(x) = (1 \times 10^{-3})[\exp(\beta x) - 1 + x^\alpha]$ . The solid black line represents the best fit of  $f(x)$  to the data. Panels (B) and (C) show the coefficients  $\beta$  and  $\alpha$  as a function of the logarithm of  $T_s$ . We observe a consistent behavior of the coefficients, with a decay as  $T_s$  increases, stabilizing for  $T_s \geq 512$ .

force increment. The detachment of these clusters constitutes an avalanche-like behavior, a phenomenon commonly observed in various natural systems such as sandpile dynamics (44), earthquakes (45), neural networks (46), and lung inflation (47–49). To evaluate the significance of collective, cluster-based fractures in the overall damage, we introduce the parameter  $\Psi$ , defined as the fraction of molecules that detach within clusters, relative to the total number of breakages observed at a given applied force. As shown in Figure 8, which presents the average results over 10 distinct fibrils for each  $T_s$  value, the evolution of  $\Psi$  reveals a strong dependence on fibril structure. For fibrils formed with low  $T_s$ , the relevance of cluster-based fractures is high even at low applied forces, indicating an inherent structural fragility. In contrast, reinforced fibrils (high  $T_s$ ) are more resilient; they initially resist collective failure, with the contribution from cluster detachments only becoming significant near the ultimate rupture force, where the fibril's failure is triggered by a final cascade of breaking clusters.

To quantitatively characterize this behavior, we define the avalanche size,  $s$ , as the cluster size, i.e., the number of molecules that detach under a fixed force. Using this definition, we calculated  $P(s)$ , the probability distribution of avalanche sizes, for each value of  $T_s$ . Our breakage model relies on statistically estimating the failure probability across various molecular conformations; for each tested  $T_s$ , we selected 10 distinct fibrils and ran 1,000 independent rupture simulations on each. The resulting distributions are shown in the inset of Fig. 9(A) on a log-log plot for  $T_s = 2$  and  $T_s = 8192$ . To characterize these distributions, we applied a scaling law (50):

$$P(s) \sim s^{-\gamma}, \quad (6)$$

where  $\gamma$  is the characteristic exponent of the power law.

The main panel in Figure 9(A) shows the scaling region of the distributions where this power-law behavior provides a good fit. Our analysis shows that for  $T_s = 2$ , the exponent is  $\gamma = 2.31$ , while for  $T_s = 8192$ , it increases to  $\gamma = 2.80$ . Between these two limits, the power-law exponent  $\gamma$  varies with  $T_s$ , as depicted in the linear-log plot in Figure 9(B). Two distinct regimes are evident: for  $T_s < 512$ , the exponent grows linearly, whereas for  $T_s \geq 512$ , it enters a plateau. This trend indicates that the avalanche size distribution becomes narrower (i.e., a higher exponent  $\gamma$ ) as  $T_s$  increases and reaches a regime of saturation, reflecting a shift in the system's mechanical response. The transition between these slopes may correspond to a change in the dominant failure mechanism due to the increased compactness of the fibril at higher values of  $T_s$  (51). A power-law distribution indicates the lack of a characteristic scale; indeed, distributions describing phenomena with a characteristic size are known to decrease exponentially. Thus, our finding of a power-law distribution for the avalanche sizes implies that the fibril rupture process is not dominated by any characteristic event size (52).

A direct consequence of avalanche-like ruptures in the fracture process should manifest as sudden stress drops in the stress-strain curve, since avalanche propagation occurs faster than the rate of strain increase (34). Although we cannot directly visualize this phenomenon in our model due to intrinsic limitations, experimental evidence strongly supports this prediction.

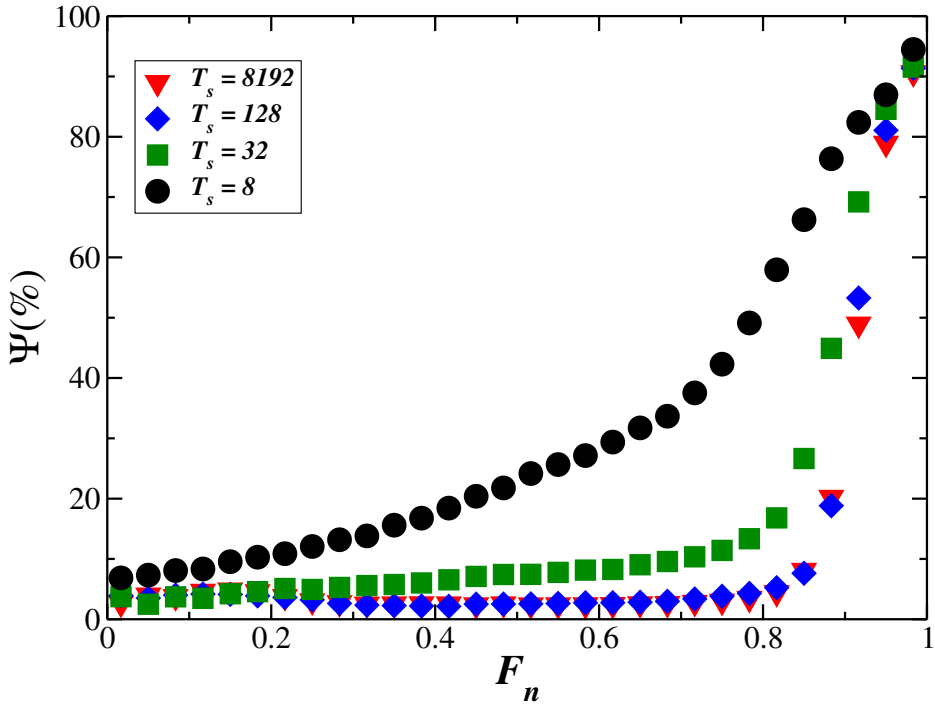


Figure 8: The average fraction of molecules removed in a cluster,  $\Psi$ , as a function of the normalized force  $F_n$  for  $T_s = 8, 32, 128$  and  $8192$ . For low  $T_s$ , cluster breakages contribute significantly even at low forces, indicating early onset of collective failure. In contrast, for high  $T_s$ , the fibril initially resists through isolated bond breaking, with cluster breakages (and catastrophic failure) occurring only near the ultimate force.

Gutsmann et al. (53) used force spectroscopy on single microfibrils and directly observed force drops caused by intermolecular cross-link ruptures. Svensson et al. (54) reported clear stress drops in tensile tests of individual collagen fibrils, while Deng et al. (24) showed similar drops in stress-strain curves. These experimental observations support the avalanche-like failure mechanism predicted by our model.

Our model is built upon significant simplifications regarding both the formation process and the subsequent mechanical behavior. In the fibrillogenesis model, collagen molecules are idealized as rigid rectangular bars, an approximation that restricts aggregation sites to the block's faces. Additionally, the molecular dynamics are simplified by confining translational diffusion to a discrete cubic lattice, thereby neglecting rotational degrees of freedom. From a physicochemical standpoint, the model also abstracts the complexity of intermolecular interactions into a single phenomenological parameter,  $T_s$ , which, while efficient, precludes a direct analysis of how fibril morphology would respond to variations in biochemical parameters such as pH or ionic strength (55). A fundamental limitation of the mechanical model lies in the probabilistic nature of fracture. This methodological choice bypasses the complexity of force transmission in a disordered structure (56, 57), but it also prevents the elucidation of specific nanomechanical mechanisms like the breakage of internal bonds. Furthermore, representing the molecules as non-deformable units is another significant simplification; by not incorporating deformation, our model cannot yield stress-strain curves, and consequently, the ultimate stress and Young's modulus cannot be calculated (58), limiting the analysis entirely to the statistics of fracture events. Despite all these simplifications, the main contribution of this work is the discovery that the rupture process is governed by a cascade of breakages exhibiting scale-free, avalanche-like behavior, and that more robust structures exhibit a higher cross-sectional fractal dimension. This work establishes a quantitative framework where the fractal dimension emerges as a key metric for mechanical resilience. It thus offers a more fundamental way to assess self-assembled biomaterials whose failure is ultimately governed by critical avalanche-like processes.

## CONCLUSION

In this work, we demonstrate that the surface diffusion parameter  $T_s$  governs both the structural compactness and mechanical resilience of collagen fibrils through a diffusion-limited aggregation model coupled with probabilistic fracture mechanics. Our key finding is that fibril rupture proceeds via an avalanche-like failure process that follows a scale-free behavior, with the fractal

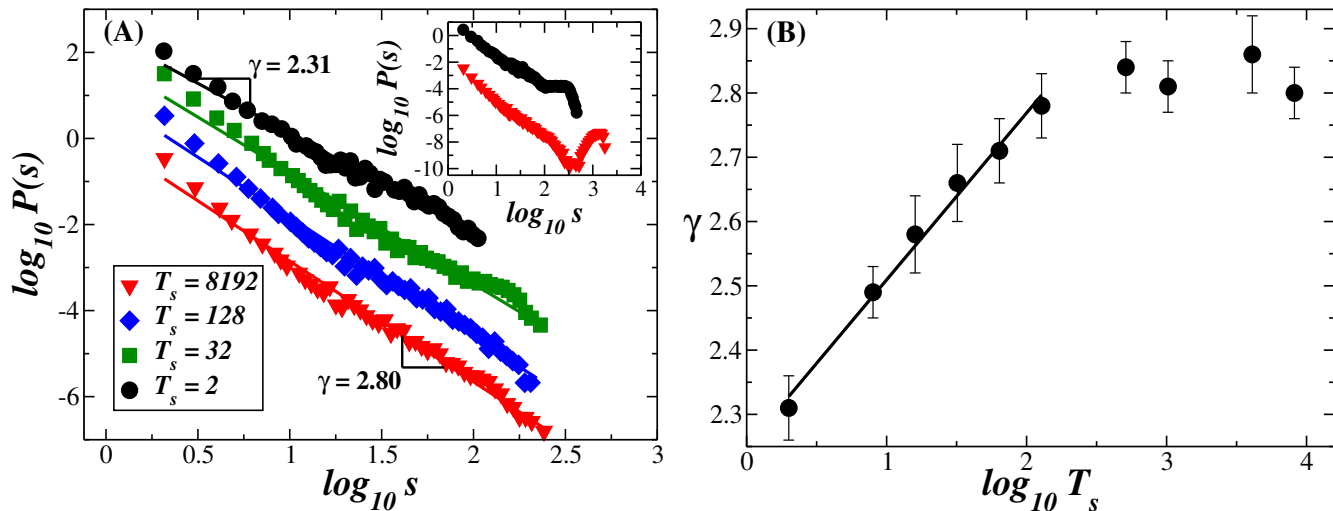


Figure 9: (A) Log-log plot of the rupture avalanche distribution,  $P(s)$ , as a function of the avalanche size  $s$  for  $T_s = 2, 32, 128$  and  $8192$ . A power-law behavior is observed, with well-defined slopes  $\gamma$  ranging from  $2.31$  to  $2.80$ . The solid lines represent the linear regression for each data set. The inset shows the full distribution, including its tail, for  $T_s = 2$  and  $T_s = 8192$ . Data sets are vertically shifted for clarity. (B) The exponent  $\gamma$  as a function of the parameter  $T_s$  on a linear-log scale. The exponent exhibits two distinct regimes: linear growth for  $T_s < 512$  (solid black line) and a plateau for  $T_s \geq 512$ .

dimension emerging as a quantitative predictor of mechanical strength. These results establish a framework for understanding how assembly conditions influence the mechanical properties of hierarchical biological materials.

## AUTHOR CONTRIBUTIONS

All authors contributed equally to this work.

## ACKNOWLEDGMENTS

We thank the Brazilian agencies CNPq, CAPES, and FUNCAP for financial support.

## REFERENCES

1. Silver, F. H., M. Jaffe, and R. G. Shah, 2018. Structure and behavior of collagen fibers. In *Handbook of Properties of Textile and Technical Fibres*, Elsevier, 345–365. <https://doi.org/10.1016/B978-0-08-101272-7.00011-0>.
2. Davison-Kotler, E., W. S. Marshall, and E. García-Gareta, 2019. Sources of collagen for biomaterials in skin wound healing. *Bioengineering (Basel)* 6:56. <https://doi.org/10.3390/bioengineering6030056>.
3. Tresoldi, I., F. Oliva, M. Benvenuto, M. Fantini, L. Masuelli, R. Bei, and A. Modesti, 2013. Tendon's ultrastructure. *Muscles Ligaments Tendons J.* 3:2–6. <https://pubmed.ncbi.nlm.nih.gov/23885339/>.
4. Fedarko, N. S., 2014. Osteoblast/Osteoclast Development and Function in Osteogenesis Imperfecta. In *Osteogenesis Imperfecta*, Elsevier, 45–56. <https://doi.org/10.1016/B978-0-12-397165-4.00005-8>.
5. Rico-Llanos, G. A., S. Borrego-González, M. Moncayo-Donoso, J. Becerra, and R. Visser, 2021. Collagen type I biomaterials as scaffolds for bone tissue engineering. *Polymers (Basel)* 13:599. <https://doi.org/10.3390/polym13040599>.
6. Chen, S., M. J. Mienaltowski, and D. E. Birk, 2015. Regulation of corneal stroma extracellular matrix assembly. *Exp. Eye Res.* 133:69–80. <https://doi.org/10.1016/j.exer.2014.08.001>.
7. Suki, B., 2021. Structure and function of the extracellular matrix. Academic Press, San Diego, CA. <https://doi.org/10.1016/C2019-0-00511-0>.

8. Amirrah, I. N., Y. Lokanathan, I. Zulkiflee, M. F. M. R. Wee, A. Motta, and M. B. Fauzi, 2022. A comprehensive review on collagen type I development of biomaterials for tissue engineering: From biosynthesis to bioscaffold. *Biomedicines* 10:2307. <https://doi.org/10.3390/biomedicines10092307>.
9. Gelse, K., E. Pöschl, and T. Aigner, 2003. Collagens—structure, function, and biosynthesis. *Adv. Drug Deliv. Rev.* 55:1531–1546. <https://doi.org/10.1016/j.addr.2003.08.002>.
10. Charvolin, J., and J.-F. Sadoc, 2019. Type-I collagen fibrils: From growth morphology to local order. *Eur. Phys. J. E Soft Matter* 42:49. <https://doi.org/10.1140/epje/i2019-11812-1>.
11. Kadler, K. E., D. F. Holmes, J. A. Trotter, and J. A. Chapman, 1996. Collagen fibril formation. *Biochem. J.* 316:1–11. <https://pubmed.ncbi.nlm.nih.gov/8645190/>.
12. Parry, D. A. D., and A. S. Craig, 1984. Growth and development of collagen fibrils in connective tissue. In *Ultrastructure of the Connective Tissue Matrix*, Springer US, Boston, MA, 34–64. [https://doi.org/10.1007/978-1-4613-2831-5\\_2](https://doi.org/10.1007/978-1-4613-2831-5_2).
13. Silver, F. H., and W. J. Landis, 2008. Viscoelasticity, energy storage and transmission and dissipation by extracellular matrices in vertebrates. In *Collagen*, Springer US, Boston, MA, 133–154. [https://doi.org/10.1007/978-0-387-73906-9\\_6](https://doi.org/10.1007/978-0-387-73906-9_6).
14. Nalbach, M., F. Chalupa-Gantner, F. Spoerl, V. de Bar, B. Baumgartner, O. G. Andriotis, S. Ito, A. Ovsianikov, G. Schitter, and P. J. Thurner, 2022. Instrument for tensile testing of individual collagen fibrils with facile sample coupling and uncoupling. *Rev. Sci. Instrum.* 93:054103. <https://doi.org/10.1063/5.0072123>.
15. van der Rijt, J. A. J., K. O. van der Werf, M. L. Bennink, P. J. Dijkstra, and J. Feijen, 2006. Micromechanical testing of individual collagen fibrils. *Macromol. Biosci.* 6:697–702. <https://doi.org/10.1002/mabi.200600063>.
16. Svensson, R. B., S. T. Smith, P. J. Moyer, and S. P. Magnusson, 2018. Effects of maturation and advanced glycation on tensile mechanics of collagen fibrils from rat tail and Achilles tendons. *Acta Biomater.* 70:270–280. <https://doi.org/10.1016/j.actbio.2018.02.005>.
17. Andriotis, O. G., M. Nalbach, and P. J. Thurner, 2023. Mechanics of isolated individual collagen fibrils. *Acta Biomater.* 163:35–49. <https://doi.org/10.1016/j.actbio.2022.12.008>.
18. Buehler, M. J., 2006. Nature designs tough collagen: explaining the nanostructure of collagen fibrils. *Proc. Natl. Acad. Sci. U. S. A.* 103:12285–12290. <https://doi.org/10.1073/pnas.0603216103>.
19. Buehler, M. J., 2006. Atomistic and continuum modeling of mechanical properties of collagen: Elasticity, fracture, and self-assembly. *J. Mater. Res.* 21:1947–1961. <https://doi.org/10.1557/jmr.2006.0236>.
20. Buehler, M. J., 2008. Molecular architecture of collagen fibrils: A critical length scale for tough fibrils. *Curr. Appl. Phys.* 8:440–442. <https://doi.org/10.1016/j.cap.2007.10.058>.
21. Buehler, M. J., 2008. Nanomechanics of collagen fibrils under varying cross-link densities: atomistic and continuum studies. *J. Mech. Behav. Biomed. Mater.* 1:59–67. <https://doi.org/10.1016/j.jmbbm.2007.04.001>.
22. Depalle, B., Z. Qin, S. J. Shefelbine, and M. J. Buehler, 2016. Large deformation mechanisms, plasticity, and failure of an individual collagen fibril with different mineral content. *J. Bone Miner. Res.* 31:380–390. <https://doi.org/10.1002/jbmr.2705>.
23. Araújo, A. D., A. Majumdar, H. Parameswaran, E. Yi, J. L. Spencer, M. A. Nugent, and B. Suki, 2011. Dynamics of enzymatic digestion of elastic fibers and networks under tension. *Proc. Natl. Acad. Sci. U. S. A.* 108:9414–9419. <https://doi.org/10.1073/pnas.1019188108>.
24. Deng, Y., J. Herrmann, Y. Wang, M. Nguyen, J. K. Hall, J. H. Kim, M. L. Smith, K. R. Lutchen, E. Bartolák-Suki, and B. Suki, 2024. Physiological mechanical forces accelerate the degradation of bovine lung collagen fibers by bacterial collagenase. *Sci. Rep.* 14:29008. <https://doi.org/10.1038/s41598-024-77704-z>.
25. Parkinson, J., K. E. Kadler, and A. Brass, 1995. Simple physical model of collagen fibrillogenesis based on diffusion limited aggregation. *J. Mol. Biol.* 247:823–831. [https://doi.org/10.1016/S0022-2836\(05\)80157-3](https://doi.org/10.1016/S0022-2836(05)80157-3).

26. Kadler, K. E., Y. Hojima, and D. J. Prockop, 1987. Assembly of collagen fibrils de novo by cleavage of the type I pro-C-collagen with procollagen C-proteinase. Assay of critical concentration demonstrates that collagen self-assembly is a classical example of an entropy-driven process. *J. Biol. Chem.* 262:15696–15701. [https://doi.org/10.1016/S0021-9258\(18\)47783-6](https://doi.org/10.1016/S0021-9258(18)47783-6).
27. García-Ruiz, J. M., and F. Otálora, 1991. Diffusion limited aggregation. The role of surface diffusion. *Physica A* 178:415–420. [https://doi.org/10.1016/0378-4371\(91\)90030-G](https://doi.org/10.1016/0378-4371(91)90030-G).
28. Mohammadkhah, M., and S. Klinge, 2023. Review: The importance of considering collagen cross-links in computational models of collagen-based tissues. *J. Mech. Behav. Biomed. Mater.* 148:106203. <https://doi.org/10.1016/j.jmbbm.2023.106203>.
29. Vicsek, T., 1991. Fractal growth phenomena (2nd edition). World Scientific Publishing, Singapore, Singapore, 2nd edition. <https://doi.org/10.1142/1407>.
30. Giordano, N. J., 2012. Computational physics. Pearson Education India. <https://www.physics.purdue.edu/~hisao/book/>.
31. Witten, T. A., and L. M. Sander, 1983. Diffusion-limited aggregation. *Phys. Rev. B Condens. Matter* 27:5686–5697. <https://doi.org/10.1103/PhysRevB.27.5686>.
32. Bažant, Z. P., and J. Planas, 2019. Fracture and size effect in concrete and other quasibrittle materials. Routledge. <https://doi.org/10.1201/9780203756799>.
33. Gilabert, A., C. Vanneste, D. Sornette, and E. Guyon, 1987. The random fuse network as a model of rupture in a disordered medium. *Journal Phys.* 48:763–770. <https://doi.org/10.1051/jphys:01987004805076300>.
34. Noguchi, H., and S. Yukawa, 2024. Fracture process of composite materials in a spring network model. *Phys. Rev. E* 110:045001. <https://doi.org/10.1103/PhysRevE.110.045001>.
35. Parkinson, J., A. Brass, G. Canova, and Y. Brechet, 1997. The mechanical properties of simulated collagen fibrils. *J. Biomech.* 30:549–554.
36. Herrmann, H. J., D. C. Hong, and H. E. Stanley, 1984. Backbone and elastic backbone of percolation clusters obtained by the new method of 'burning'. *J. Phys. A Math. Gen.* 17:L261–L266. <https://iopscience.iop.org/article/10.1088/0305-4470/17/5/008>.
37. Moreira, A. A., C. L. N. Oliveira, A. Hansen, N. A. M. Araújo, H. J. Herrmann, and J. S. Andrade, Jr, 2012. Fracturing highly disordered materials. *Phys. Rev. Lett.* 109:255701. <https://doi.org/10.1103/PhysRevLett.109.255701>.
38. Vater, C. A., E. D. Harris, Jr, and R. C. Siegel, 1979. Native cross-links in collagen fibrils induce resistance to human synovial collagenase. *Biochem. J.* 181:639–645. <https://doi.org/10.1042/bj1810639>.
39. Jones, D. R., and M. F. Ashby, 2012. Engineering materials 2: an introduction to microstructures and processing. Butterworth-Heinemann. <https://doi.org/10.1016/C2009-0-64289-6>.
40. Buehler, M. J., and Y. C. Yung, 2009. Deformation and failure of protein materials in physiologically extreme conditions and disease. *Nat. Mater.* 8:175–188. <https://doi.org/10.1038/nmat2387>.
41. Veres, S. P., J. M. Harrison, and J. M. Lee, 2013. Repeated subrupture overload causes progression of nanoscaled discrete plasticity damage in tendon collagen fibrils. *J. Orthop. Res.* 31:731–737. <https://doi.org/10.1002/jor.22292>.
42. Zapperi, S., P. Ray, H. E. Stanley, and A. Vespignani, 1997. First-order transition in the breakdown of disordered media. *Phys. Rev. Lett.* 78:1408–1411. <https://doi.org/10.1103/PhysRevLett.78.1408>.
43. Zapperi, S., P. Ray, H. E. Stanley, and A. Vespignani, 1999. Avalanches in breakdown and fracture processes. *Phys. Rev. E Stat. Phys. Plasmas Fluids Relat. Interdiscip. Topics* 59:5049–5057. <https://doi.org/10.1103/PhysRevE.59.5049>.
44. Jaeger, H. M., and S. R. Nagel, 1992. Physics of the granular state. *Science* 255:1523–1531. <https://doi.org/10.1126/science.255.5051.1523>.

45. Godano, C., M. L. Alonso, and V. Caruso, 1993. Self-organized criticality and earthquake predictability. *Phys. Earth Planet. Inter.* 80:117–123. [https://doi.org/10.1016/0031-9201\(93\)90042-8](https://doi.org/10.1016/0031-9201(93)90042-8).
46. Beggs, J. M., and D. Plenz, 2003. Neuronal avalanches in neocortical circuits. *J. Neurosci.* 23:11167–11177. <https://pmc.ncbi.nlm.nih.gov/articles/PMC6741045/>.
47. Barabási, A. L., S. V. Buldyrev, H. E. Stanley, and B. Suki, 1996. Avalanches in the lung: A statistical mechanical model. *Phys. Rev. Lett.* 76:2192–2195. <https://doi.org/10.1103/PhysRevLett.76.2192>.
48. Alencar, A. M., S. V. Buldyrev, A. Majumdar, H. E. Stanley, and B. Suki, 2001. Avalanche dynamics of crackle sound in the lung. *Phys. Rev. Lett.* 87:088101. <https://doi.org/10.1103/physrevlett.87.088101>.
49. Suki, B., A. L. Barabási, Z. Hantos, F. Peták, and H. E. Stanley, 1994. Avalanches and power-law behaviour in lung inflation. *Nature* 368:615–618. <https://doi.org/10.1038/368615a0>.
50. Zapperi, S., A. Vespignani, and H. E. Stanley, 1997. Plasticity and avalanche behaviour in microfracturing phenomena. *Nature* 388:658–660. <https://doi.org/10.1038/41737>.
51. Zhao, Y., M. Chen, X. Jiang, X. Cao, and B. Qin, 2025. Damage evolution and avalanche characteristics of concrete under salt-freezing action by acoustic emission. *Developments in the Built Environment* 21:100600. <https://doi.org/10.1016/j.dibe.2024.100600>.
52. Bak, P., C. Tang, and K. Wiesenfeld, 1987. Self-organized criticality: An explanation of the 1/f noise. *Phys. Rev. Lett.* 59:381–384. <https://doi.org/10.1103/PhysRevLett.59.381>.
53. Gutsmann, T., G. E. Fantner, J. H. Kindt, M. Venturoni, S. Danielsen, and P. K. Hansma, 2004. Force spectroscopy of collagen fibers to investigate their mechanical properties and structural organization. *Biophys. J.* 86:3186–3193. [https://doi.org/10.1016/S0006-3495\(04\)74366-0](https://doi.org/10.1016/S0006-3495(04)74366-0).
54. Svensson, R. B., H. Mulder, V. Kovanen, and S. P. Magnusson, 2013. Fracture mechanics of collagen fibrils: influence of natural cross-links. *Biophys. J.* 104:2476–2484. <https://doi.org/10.1016/j.bpj.2013.04.033>.
55. Jiang, F., H. Hörber, J. Howard, and D. J. Müller, 2004. Assembly of collagen into microribbons: effects of pH and electrolytes. *J. Struct. Biol.* 148:268–278. <https://doi.org/10.1016/j.jsb.2004.07.001>.
56. Ruiz-Franco, J., and J. van Der Gucht, 2022. Force transmission in disordered fibre networks. *Front. Cell Dev. Biol.* 10:931776. <https://doi.org/10.3389/fcell.2022.931776>.
57. Provenzano, P. P., and R. Vanderby, Jr, 2006. Collagen fibril morphology and organization: implications for force transmission in ligament and tendon. *Matrix Biol.* 25:71–84. <https://doi.org/10.1016/j.matbio.2005.09.005>.
58. Innocenti, B., and F. Galbusera, editors, 2022. Human orthopaedic biomechanics. Academic Press, San Diego, CA. <https://www.sciencedirect.com/book/edited-volume/9780128244814/human-orthopaedic-biomechanics>.